DSCOVR EPIC and NISTAR STM (GSFC, Bld. 33, H114)

Andrew Lacis and Barbara Carlson

NASA Goddard Institute for Space Studies New York, NY

Goddard Space Flight Center
Greenbelt, MD

September 17 – 18, 2018

Radiative Forcing of Seasonal Earth Radiation Imbalance

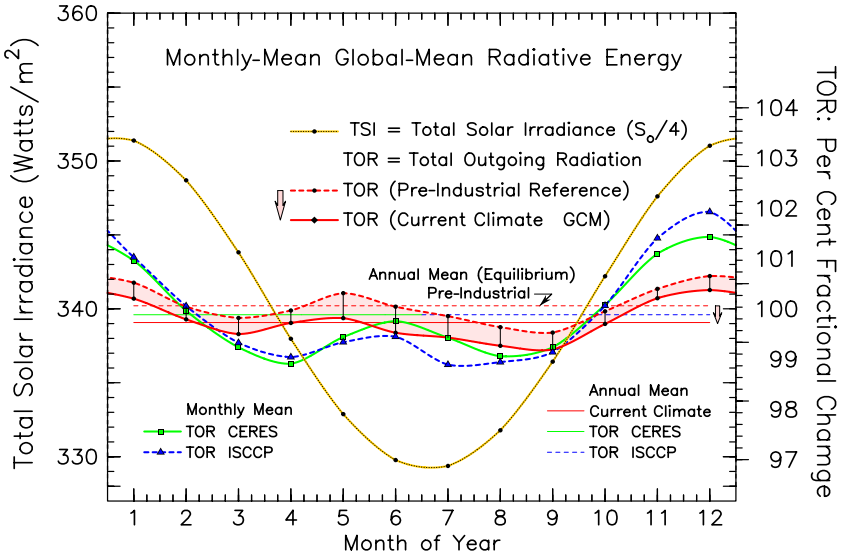

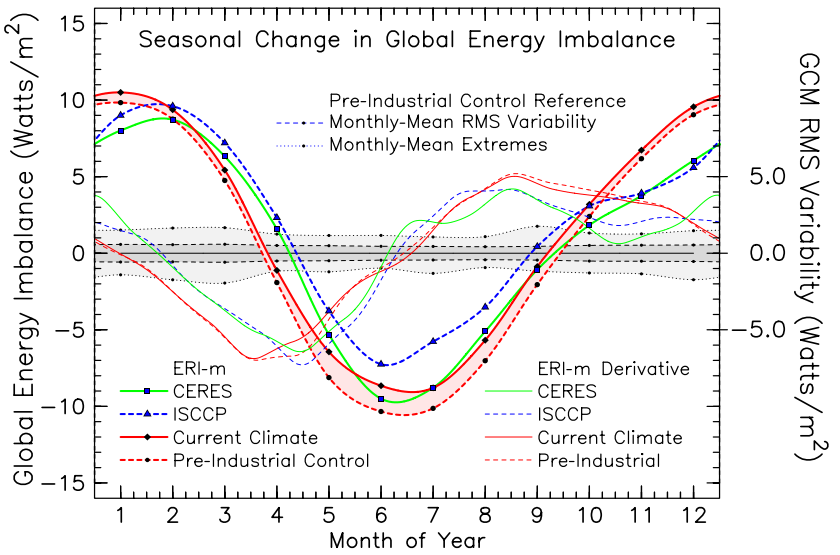

Since total energy has to be conserved at every grid-box and time-step, the observed *Seasonal Change* in Total Solar Irradiance, **TSI**, and the Total Outgoing Radiation, **TOR**, serve as fundamental observational constraints on climate **GCM** performance. **TSI** is measured with high accuracy ($S_o/4$ annual-mean = 340.2 W/m^2). Earth's orbital motion induces a precisely known seasonal SW (peak-to-peak 22 W/m^2) radiative forcing that drives the seasonal climate change. **TOR** is a much more difficult measurement (**CERES**, green curve; **ISCCP**, blue-dash curve), and is in need of improved accuracy. **TOR** is also a difficult calculations, requiring a comprehensive climate **GCM** (red-dash curve for pre-industrial (1850) climate conditions; solid red for current (2000 – 2010) climate conditions. The right panel depicts the global Earth Radiation Imbalance, **ERI = TSI – TOR**, which, for the GISS ModelE2, has produced a 1.1 W/m^2 annual-mean imbalance (between 1850 and 2010) in response to the accumulated greenhouse gas radiative forcing. Also shown in gray-scale is the 1 and 2 **σ** RMS natural variability of the **GCM** computed global-mean **ERI**.

Solar Seasonal SW Forcing of the Global GCM TOR

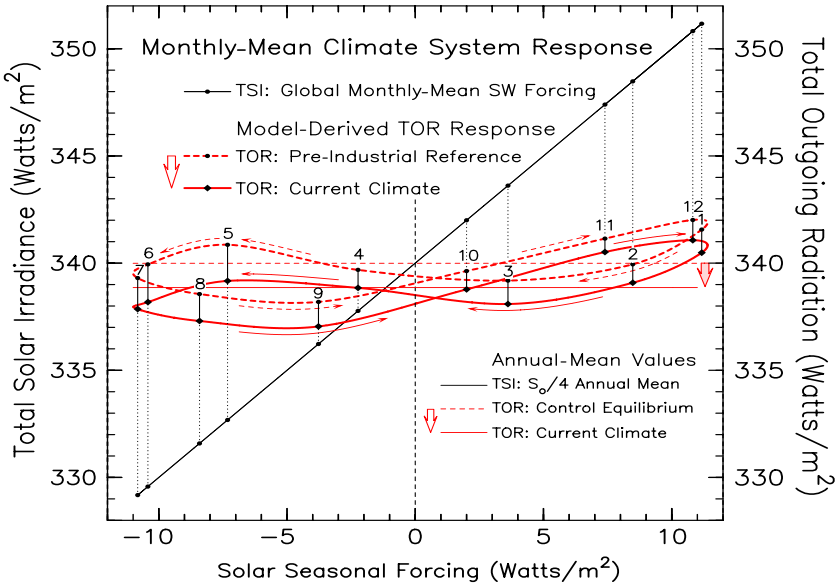

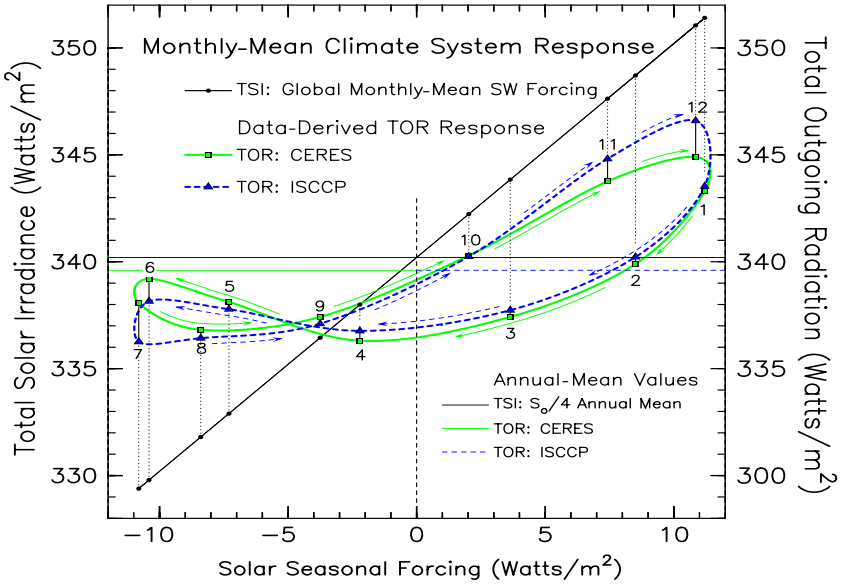

Given that the seasonal SW radiative forcing is precisely known in both time and magnitude, the Solar Seasonal Forcing can be used as the X-axis to plot both SW **TSI** (using the left-hand Y-axis), and the **GCM**-generated **TOR** (using the right-hand Y-axis) to produce the 'pinwheel'-type format for the climate system response to the seasonal SW forcing. The SW **TSI** retraces itself precisely in going from its +11 W/m^2 maximum in January, to its – 11 W/m^2 minimum in July, and back. The pinwheel format shows explicitly the GCM **TOR** phase lag and hysteresis response to SW seasonal forcing, reflecting the complexities of the ocean heat energy sequestration during the NH winter months, meridional transport patterns, and the release back to the atmosphere during NH summer months. The basic figure-8 pattern of the **GCM** pinwheel exhibits little change in going from 1850 to 2010, suggesting that basic atmosphere and ocean circulation patterns have remained stable. The right-hand panel depicts the seasonal changes in **TOR** for the corresponding **CERES** and **ISCCP** observation-based results. The close **CERES/ISCCP** agreement is not accidental, with both results normalized in accord with the Stephens *et al*. [2012] 0.6 W/m^2 **ERI** determination. The cause or significance of the slope and lobe difference is not understood.

Solar Seasonal SW Forcing of Reflected SW Radiation

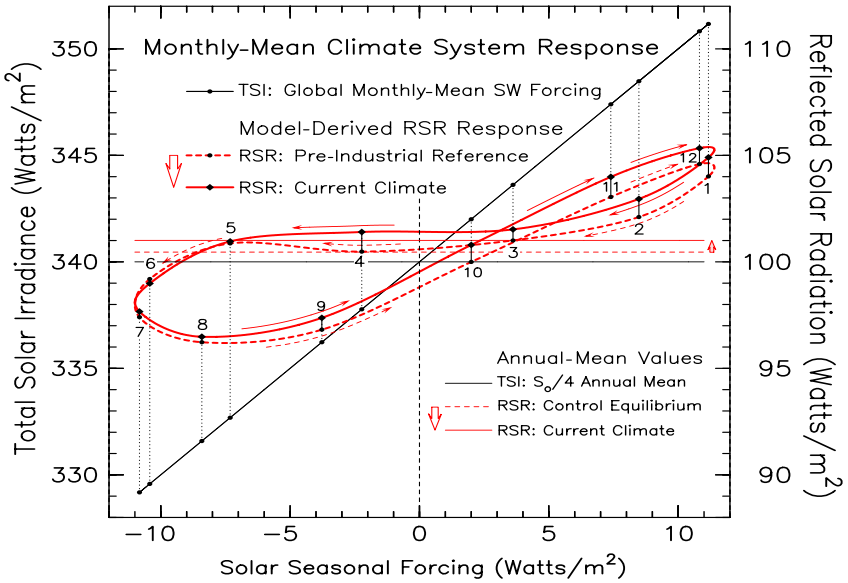

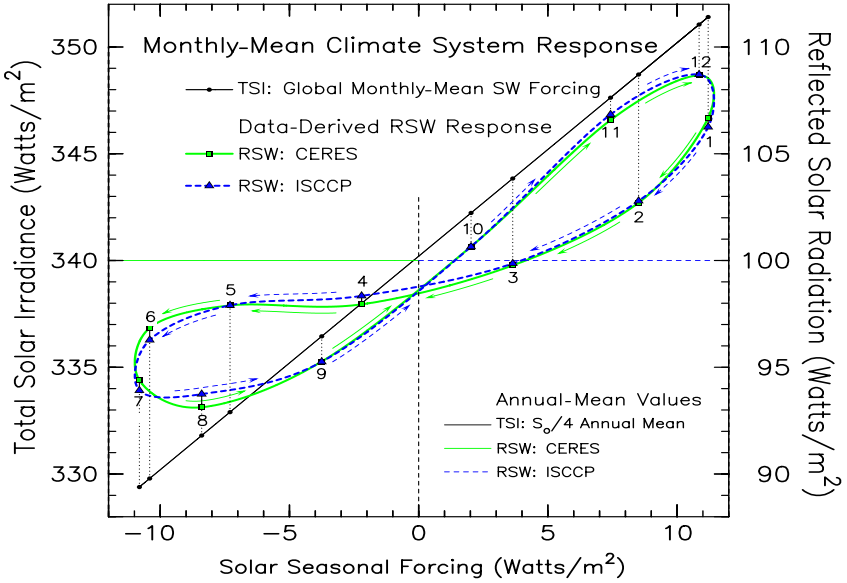

GCM diagnostics are designed to reproduce a broad range of climate variables for comparison to corresponding observational data. These include the Reflected Solar Radiation **RSR** (left-hand panel). These results show a noticeable increase in slope of the **GCM RSR** pinwheel along with a substantial decrease in the size of the NH winter lobe. Interestingly, the **GCM** generated **RSR** change from pre-industrial to current climate (1850 – 2010) conditions is a *decrease* **RSR** by about 0.5 W/m^2, with hardly any of this **RSR** change occurring during the NH summer months. The right-hand panel shows the corresponding pinwheel diagrams for the **CERES** & **ISCCP** data for current climate conditions. The annual means of the **CERES** & **ISCCP RSW** data have been normalized to 100 W/m^2 in accord with the Stephens *et al* [2012] analysis. The **CERES** & **ISCCP RSW** pinwheels exhibit a slope much more strongly aligned with the **TSI** radiative forcing slope with nearly equal sized lobes compared to the **TOR** pinwheel results. Given their very different basis (**CERES** is empirical angle model dependent, while **ISCCP** is based on cloud property and surface albedo retrievals, TOVS temperature and water vapor profiles, and radiative model calculations), it is remarkable that **CERES** and **ISCCP** agree as well as they do.

Solar Seasonal SW Forcing of Outgoing LW Radiation

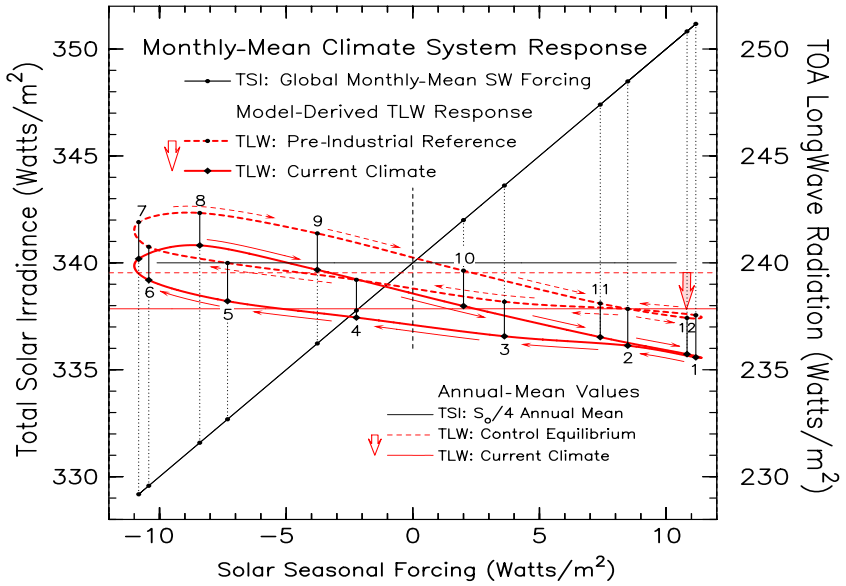

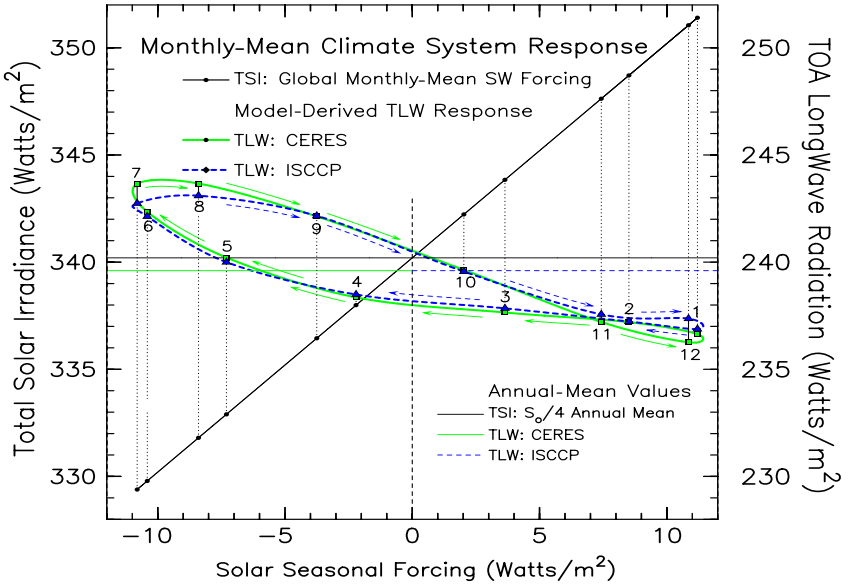

For the top-of-the-atmosphere outgoing longwave, **TLW**, radiation, the **GCM** and **CERES** & **ISCCP** pinwheel diagrams appear to agree remarkably well in both shape and slope, including also a greatly diminished NH winter hemisphere lobe. It is also of interest that the slope of the **TLW** pinwheels is contrary to common sense expectation. It is seen that as the global-mean SW radiative forcing decreases from its maximum value in January, the outgoing LW flux increases, reaching its near-maximum value in July (August is the actual maximum) when the SW radiative forcing is at its minimum. The reason for this seemingly contrary behavior is the slow temperature response of the ocean compared to the fast temperature response of the land. During the NH winter months, solar SW energy is being sequestered in SH oceans (with little temperature response). Then during NH summer months, the land warms, increasing the outgoing **TLW** radiation, even though the seasonal **TSI** radiative forcing is at its minimum, thus causing the **ERI** to be running a deficit. In order to make all this happen, a comprehensive coupled atmosphere-ocean model is required.

Seasonal Change in Surface Temperature & Cloud Cover

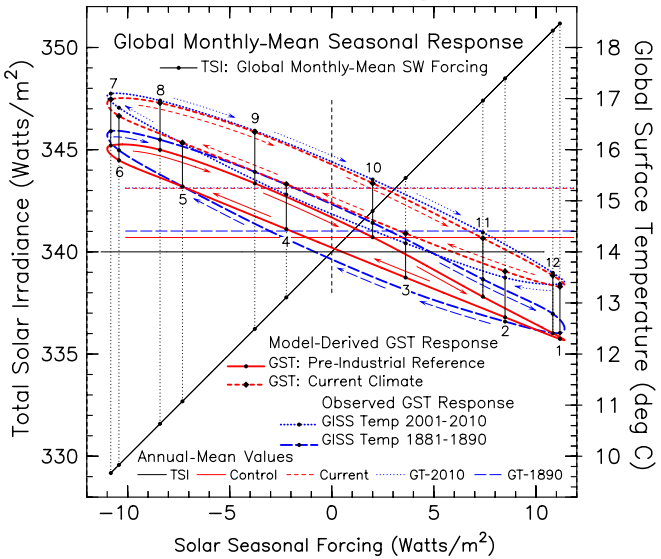

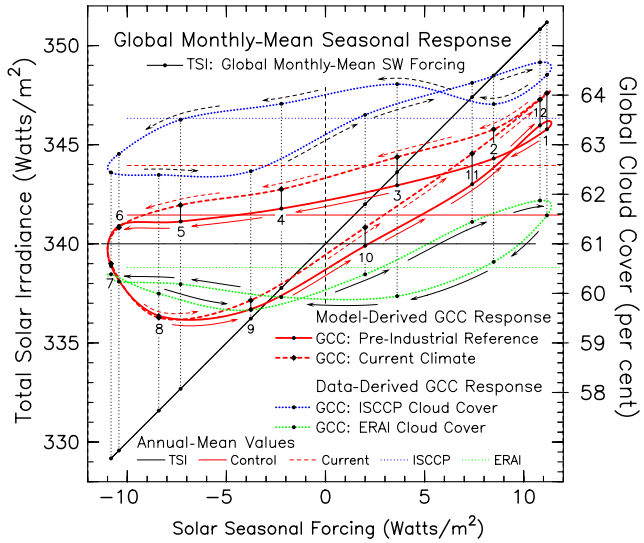

Displayed here are additional **GCM** diagnostics in pinwheel format that are relevant to the **TOR**, **RSW**, and **TLW** radiative flux seasonal change diagnostics. The left-hand panel compares the **GCM**-generated global-mean surface temperature changes from pre-industrial to current climate conditions with the observed surface temperature record (**GISTEMP** data for 18881 – 1890, and 2001 – 2010). The corresponding pinwheel plots show close agreement, but without a tendency for a figure-8 configuration. However, since the surface temperature and outgoing LW flux are closely related, the pinwheel slope is significant, being similar to the **TLW** pinwheel slope for both **GCM** and **CERES/ISCCP**, even though the slopes appear contrary to the direction of the solar SW radiative forcing. The contrary slope arises from the hemispheric land/ocean distribution, with energy being sequestered in SH oceans during the NH winter, then released during NH summer as the land surface warms, while running a global energy deficit. The right-hand panel shows the seasonal cloud variability in pinwheel format. Clouds are problematic. Model *vs* data, as well as data *vs* data, are in only qualitative agreement. The disagreement between the **GCM** and **CERES/ISCCP RSW** pinwheels could be due to differences in seasonal cloud fraction, cloud optical depth, or cloud diurnal change between **GCM** clouds and the real world. **EPIC** cloud data could help decide this uncertainty.

Can NISTAR Adjudicate GCM & CERES and ISCCP ?

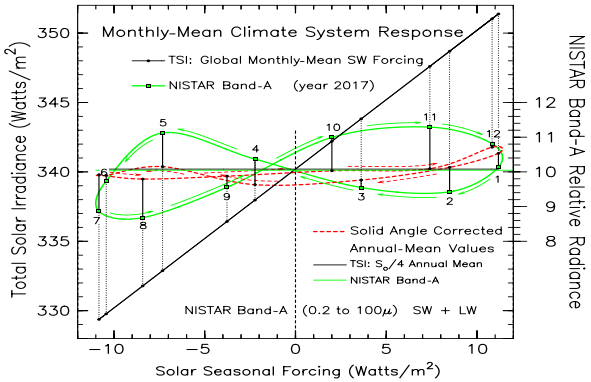

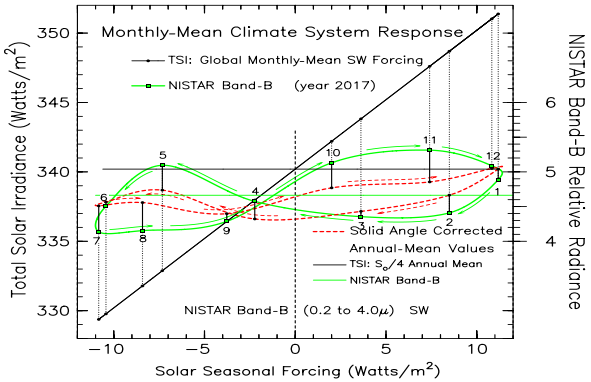

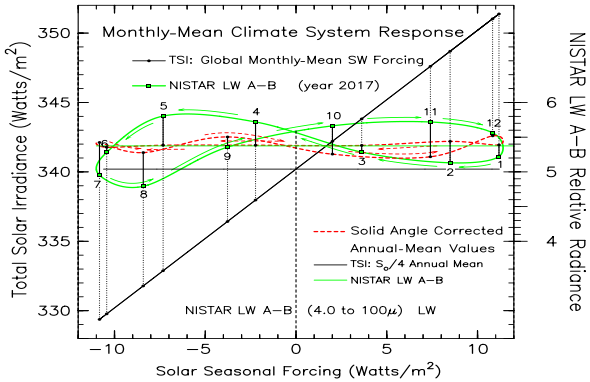

Initial pinwheel plots (green curves) of the **NISTAR** L-1B for the year-2017 for Band-A, Band-B, and of the difference Band-A – Band-B corresponding to the **TOR**, **RSW**, and **TLW** plots for **GCM**, **CERES**, and **ISCCP** data looked very promising, until it became clear that the amplitude of the seasonal variability was far too large. Accounting for the Earth-Satellite distance (Earth-disk solid angle) produces the red dash curves, which have similarity in slope and amplitude of the seasonal variability, but otherwise are significantly different from the **GCM**, **CERES**, and **ISCCP** pinwheel figures. There a number of major reasons for the differences: (1) since **NISTAR** views only the dayside hemisphere, more than twice the reflected SW radiation is present in the **NISTAR** Band-A and Band-B data compared to **GCM**-type global mean data; (2) because of the **DSCOVR** Lissajous orbit, the illuminated disk fraction for SW radiation is different from the whole disk image for LW radiation; (3) because of the Lissajous orbit, there is a latitude shift in the latitude sampling of the Earth that is different from the GCM-type global averaging; (4) from the Lagrangian L-1 point, **NISTAR** aggregates near-backscatter SW radiances and LW emission angles that differ significantly from the GCM-type radiative flux averages; (5) because of the need to correct Band-B data for filter transmission before subtracting from Band-A to obtain the **NISTAR** LW measurement, and because of the possible spill-over of SW radiation beyond the 3.5 µm Band-B cut-off, there remain uncertainties in the purity of the LW data.

GCM, CERES, ISCCP vs NISTAR on TOR, SW, LW

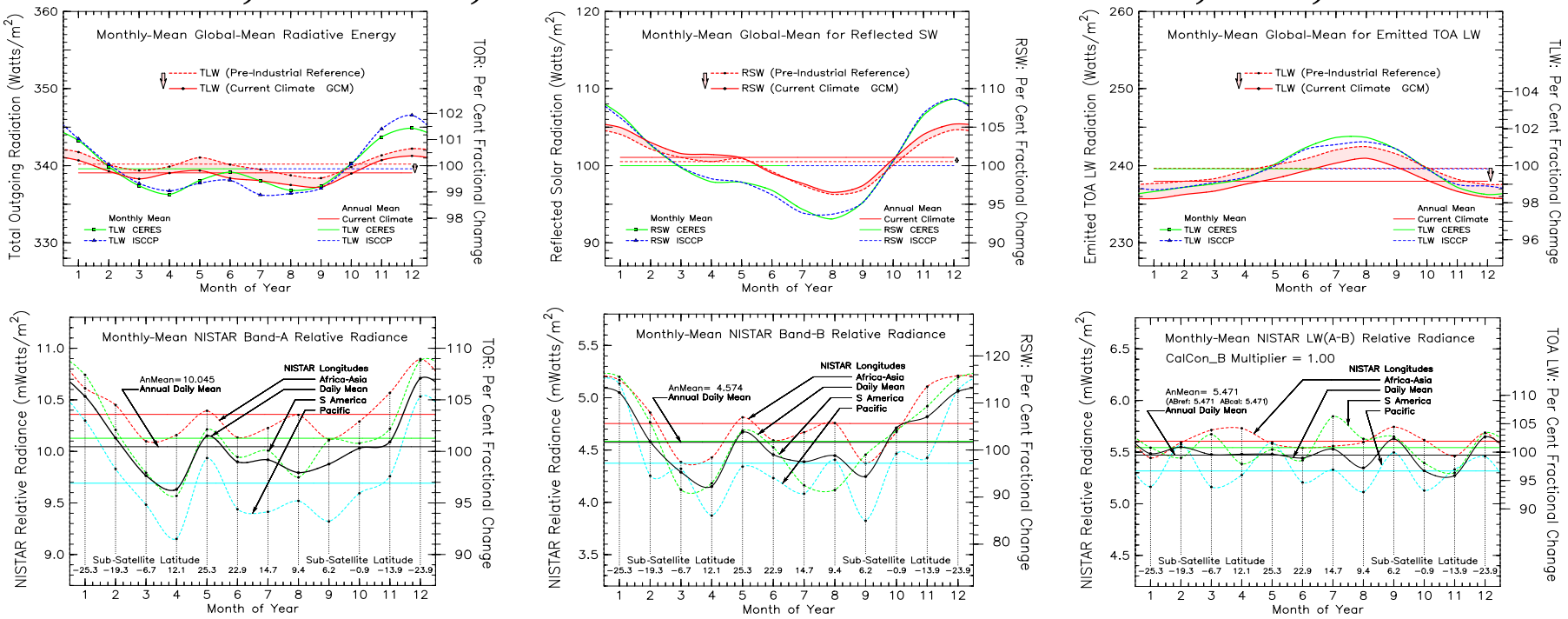

Seasonal variability in time dependent format of **TOR**, **RSW**, and **TLW** as obtained from **GCM**, **CERES**, and **ISCCP** data (top panels), with the corresponding seasonal variability as seen by **NISTAR** (bottom panels). Most notable is the strong diurnal variability that is seen in the **NISTAR** Band-A, Band-B, and Bands[A – B] data. Such diurnal variability, while implicitly present in the **GCM**, **CERES**, and **ISCCP** data streams, it has seldom been examined in the seasonal format of the **NISTAR** panels. Some of the seasonal fluctuations in **NISTAR** seasonal changes are due to the latitudinal shifting in NISTAR viewing perspective arising from the Lissajous orbit. Also, some of the fluctuations may well be due to inconsistencies in constructing the monthly mean averages from mismatched L-1B data selected for this study. This also shows that **GCM** 3D flux data need to be transformed to the **EPIC/NISTAR** 2D format for effective comparison.

Seasonal Dependence of NISTAR TOR, SW, and LW Data

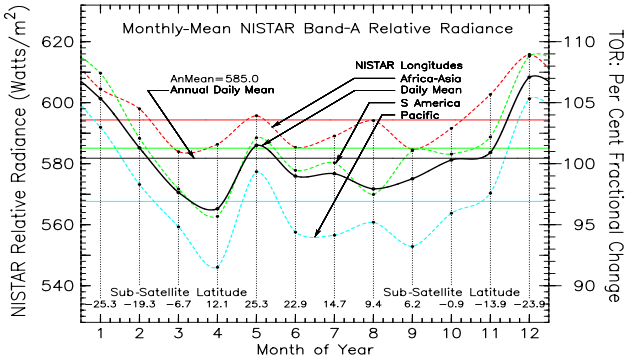

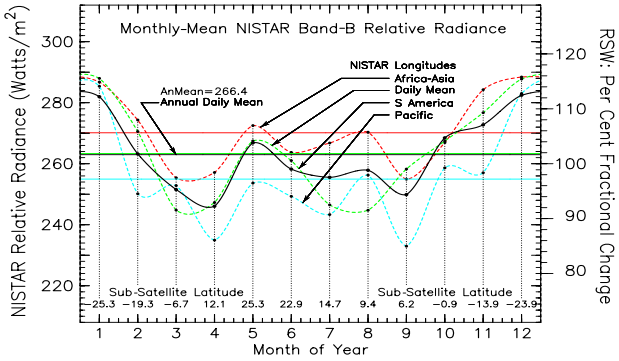

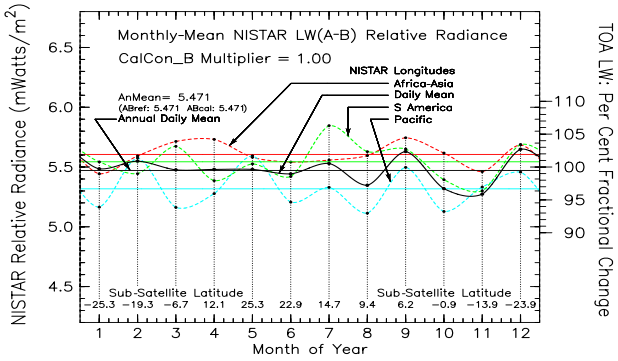

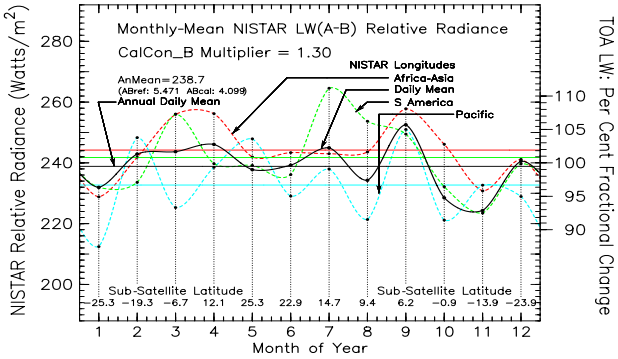

A crude example in using the seasonal variability of the **TLW** to 'calibrate' the **NISTAR** Band-B SW flux is illustrated in the right-hand panels. Seasonal variability of **NISTAR** data (daily mean, heavy black line) is complex because of the Lissajous latitude-shift of the **NISTAR** viewing geometry, and perhaps also by the near-backscatter SW radiance. For a meaningful comparison of the seasonal variability between **GCM, CERES/ISCCP** type data, and the NISTAR measurements requires not only transformation from **GCM** 3D to **EPIC/NISTAR** 2D format, but also a conversion of **GCM**-type flux data into radiances with the appropriate SW near-backscatter dependence and LW emission angles. Then, by adjusting the magnitude of the Band-B SW multiplier (1.3 in the bottom panel) to account for Band-B filter transmission and potential spill-over of SW radiation beyond the 3.5 μm Band-B cut-off until the patterns of seasonal variability between **GCM, CERES/ISCCP** and **NISTAR** Bands[A – B], all SW radiation form Band-A would have been eliminated, allowing for equating the global mean **TLW** fluxes, and thus effect a **NISTAR** LW calibration.

Implications of NISTAR Band-C / Band-B Spectral Ratio

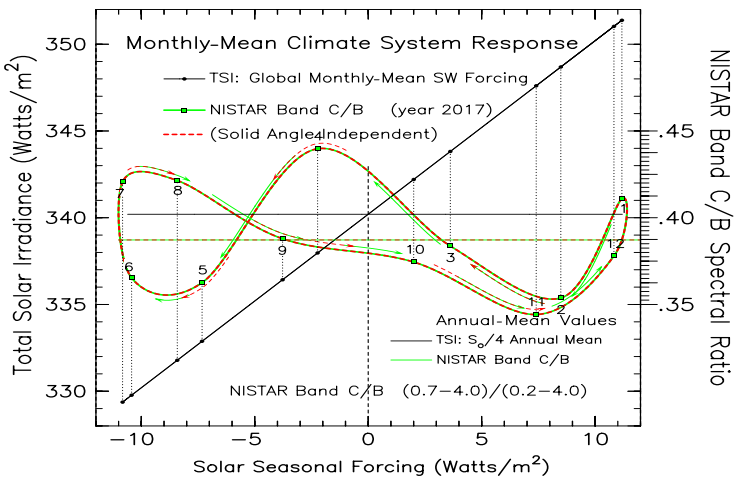

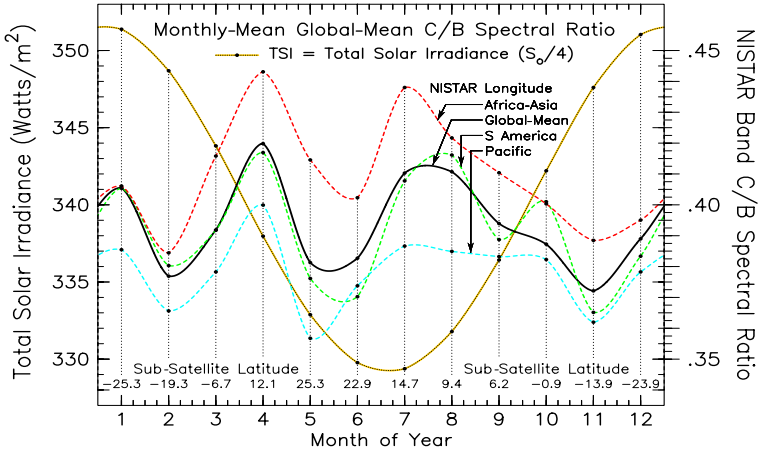

As evident from the complex pinwheel plot in the left-hand panel, the physical quantity represented by the **NISTAR** Band-C / Band-B spectral ratio is clearly not a meaningful function of the seasonal SW radiative forcing. What then is it a function of? The **NISTAR** spectral split at 0.7 µm makes the **NISTAR** C/B ratio a very powerful discriminator of the spectral dependence of climate system constituents. Cloud, snow/ice albedo decreases strongly with wavelength, while vegetation albedo increases. Ocean albedo is spectrally flat and low, desert albedo is spectrally flat and high. This makes the **NISTAR** C/B ratio sensitive to land/ocean differences in the visible hemisphere. The right-hand panel shows the **NISTAR** C/B ratio in time dependent form (heavy black line for daily mean, the red-dash for Africa-Asia longitudes, blue-dash for Pacific longitudes, and green-dash for S. America longitudes). The seasonal change in the amplitude of the diurnal variability, and the seasonal change in Band-B and Band-C magnitude can be used to identify the dominant form of surface-type in that particular **NISTAR** hemispheric view. Since **NISTAR** views the Earth in much the same way as an exoplanet seen from a near-by star system, the broadband **NISTAR** C/B spectral ratio would be an effective observational strategy to infer diurnal and seasonal biosphere information from a time-series of broadband spectral ratio measurements.

Additional Examples of NISTAR Spectral Ratio Variability

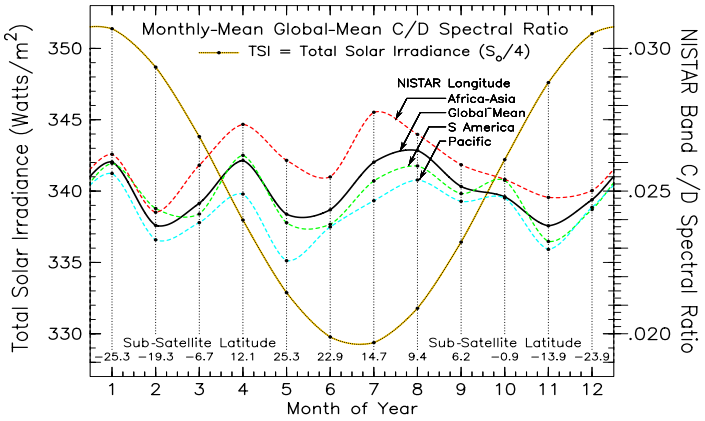

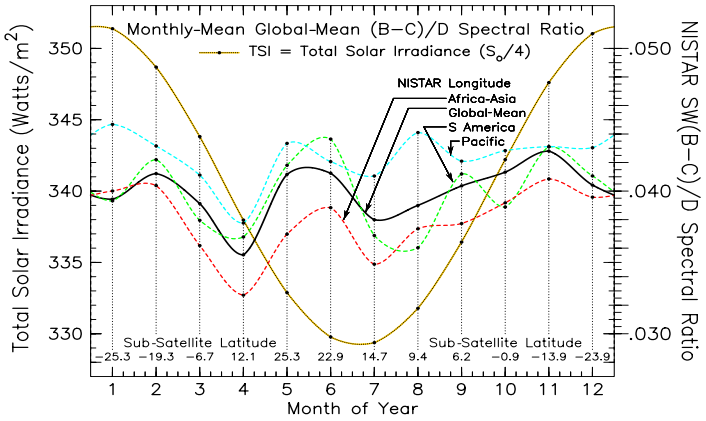

There is additional spectral ratio information available from **NISTAR** data to help differentiate between the different climate system constituents. For example, The **NISTAR** C/D spectral ratio has the SWuv (0.2 – 0.7 µm) component subtracted out in the numerator (left panel). That is why here the Africa-Asia longitudes (red dash) exhibit a higher ratio than the Pacific longitudes (blue dash). On the other hand, the **NISTAR** [B-C]/D ratio, has only the SWuv (0.2 – 0.7 µm) component in the numerator (right panel). This produces a higher spectral ratio for the Pacific longitudes (blue dash), and a lower ratio for the Africa-Asia longitudes (red dash). Clouds over the Pacific (with high albedo in the 0.2 – 0.7 µm region) account for any high reflectivity seen in the Pacific-longitude hemisphere, while the Africa-Asia vegetated land areas get high reflectivity in the 0.7 – 4.0 µm spectral region. The strong diurnal and seasonal variability seen in **NISTAR** spectral-band ratios is strongly diagnostic of **GCM** spectral albedo modeling. Moreover, these spectral ratios are robust in that they do not depend on the Earth-Satellite distance changes, or on the SW illuminated fraction of the **NISTAR**-visible disk. These are just some of the examples of what might be learned from similar broadband spectral ration exoplanet observations.

Cloud Radiative Properties are the Source of All Problems

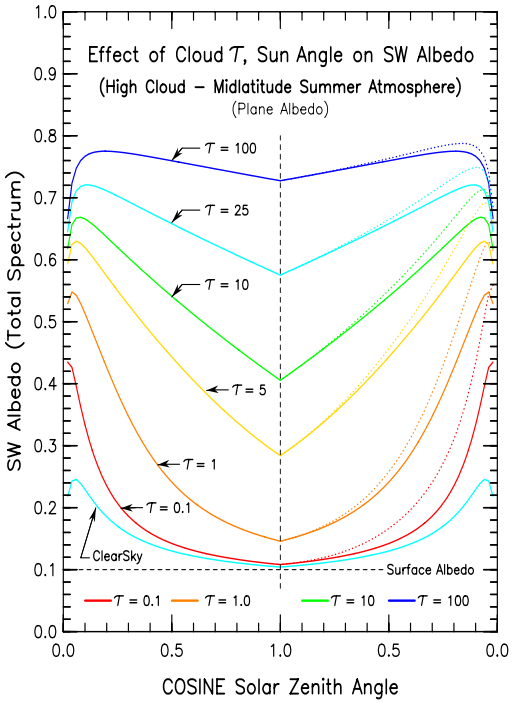

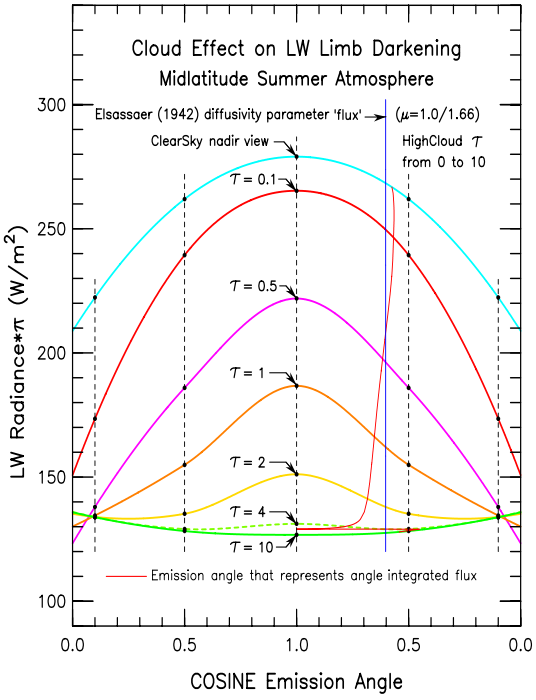

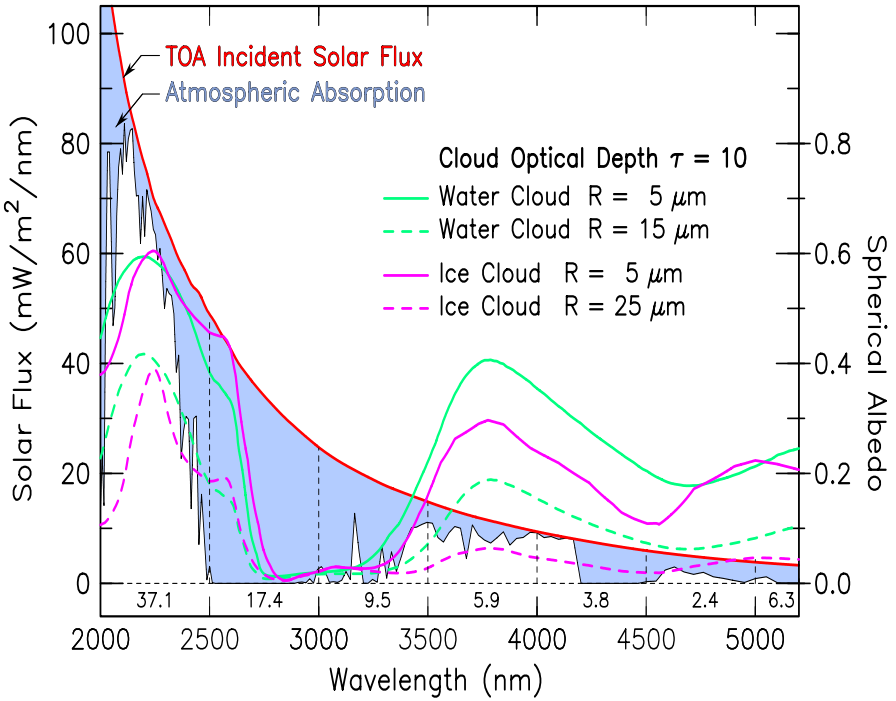

The fiendish radiative properties of clouds make it very problematic to deduce the SW and LW global energy of the Earth with demonstrable accuracy at the 1 Wm^{-2} level. **ISCCP** aggregates pixel-level data points based on cloud retrievals, TOVS data, and radiation model calculations to generate their global energy product). Similarly, **CERES** utilizes empirical SW and LW angle models that are derived from satellite based cloud-retrieval information. The above panels illustrate the SW albedo, LW flux (including LW radiance), and the near-IR spectral dependence on cloud optical depth, particle size, and water/ice phase from the **GCM** perspective. What is needed for meaningful comparison to **NISTAR** data is to transform the above radiative flux quantities into corresponding radiances for the near-backscatter **NISTAR**-view geometry.